ACS APPLIED MATERIALS & INTERFACES

Research Article

www.acsami.org

Temperature Dependence of Oxygen Reduction Reaction Activity at Stabilized Pt Skin-PtCo Alloy/Graphitized Carbon Black Catalysts Prepared by a Modified Nanocapsule Method

Kazuki Okaya,[†] Hiroshi Yano,[‡] Katsuyoshi Kakinuma,[‡] Masahiro Watanabe,[‡] and Hiroyuki Uchida*[,‡,§]

[†]Interdisciplinary Graduate School of Medicine and Engineering, [‡]Fuel Cell Nanomaterials Center, and [§]Clean Energy Research Center, University of Yamanashi, Miyamae 7-32, Kofu 400-8511, Japan

Supporting Information

ABSTRACT: We have developed a new catalyst supported on graphitized carbon black (GCB), which exhibits higher resistance to carbon corrosion than a conventional carbon black (CB), in order to favor both high mass activity for the oxygen reduction reaction (ORR) and high durability. To protect the underlying Pt_XCo alloy from corrosion and maintain the modified electronic structure, two monolayers of Pt-skin layer ($Pt_{2\ ML}$) were formed on the Pt_XCo core-particles, which were of uniform size and composition. Characterization of the $Pt_{2\ ML}$−PtCo(X = 1)/GCB, both by a scanning transmission electron microscope (STEM) with an energy dispersive X-ray (EDX) analyzer and by X-ray diffraction (XRD), indicated the formation of the $Pt_{2\ ML}$ on the PtCo alloy solid solution nanoparticles. The temperature dependence of the ORR activity of the $Pt_{2\ ML}$−$PtCo_{(2\ nm)}$/GCB catalyst was evaluated from the hydrodynamic voltammograms in O_2-saturated 0.1 M $HClO_4$ solution at 30−90 °C by the channel flow double electrode (CFDE) technique. It was found that the Co dissolution from PtCo particles during the ORR was considerably suppressed by the stabilized Pt-skin structure. The kinetically controlled mass activity (MA_k) for the ORR at the $Pt_{2\ ML}$−$PtCo_{(2\ nm)}$/GCB at E = 0.85 V vs reversible hydrogen electrode (RHE) was about two times larger than that for a standard commercial c-Pt/CB catalyst at 80−90 °C. The value of H_2O_2 yield at the $Pt_{2\ ML}$−$PtCo_{(2\ nm)}$/GCB was found to be very low (0.2%), about one-half of that for c-Pt/CB, and it is thus better able to mitigate the degradation of the polymer electrolyte membrane and gasket material.

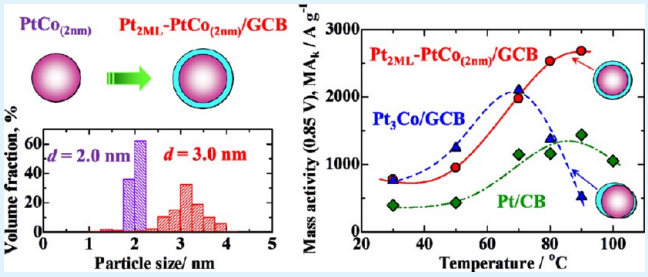

KEYWORDS: *polymer electrolyte fuel cell, electrocatalyst, PtCo alloy, Pt-skin, oxygen reduction reaction*

INTRODUCTION

Polymer electrolyte fuel cells (PEFCs) have been developed intensively for applications in fuel cell electric vehicles (FCEVs) and residential cogeneration systems. At present, the cathode catalysts of PEFCs require an appreciable amount of costly platinum or its alloys, due to the slow kinetics of the oxygen reduction reaction (ORR) in an acidic environment at low operating temperatures <100 °C. For reasons of cost and supply limitation related to near-term large-scale commercialization, it is very important to reduce the amount of Pt by developing new catalysts, coping with both high ORR activity and high durability.

The mass activity (MA) of a Pt-based catalyst for the ORR is defined as follows:

$$\mathrm{MA}\ (\mathrm{A\,g_{Pt}^{-1}}) = j_S\ (\mathrm{A\,m^{-2}}) \times \mathrm{ECA}\ (\mathrm{m^2 g_{Pt}^{-1}}) \quad (1)$$

where j_S is the specific activity (current density per active surface area) for the ORR and ECA is the electrochemically active surface area. It has been reported for planar electrodes in acid electrolyte solutions that the values of j_S were enhanced at Pt alloyed with nonprecious metal elements such as Fe,[1−5] Co,[1,3,5−10] Ni,[1,3,4,6−9,11−13] Mn,[1] Cr,[6−8,10,14,15] and V.[16] We first demonstrated that nonprecious metal elements in Pt−Fe, Pt−Co, and Pt−Ni alloys were leached out in acidic solution, followed by a spontaneous formation of a "Pt-skin layer" with a modified electronic structure on the alloy surface, resulting in the increase in the ORR activity.[2,3,12,17−23]

To increase the ECA, it is usually effective to disperse Pt or Pt-alloy nanoparticles on high surface area supports such as carbon black (CB). We also succeeded in preparing monodisperse Pt_XCo (atomic ratio X = 1, 2, and 3) alloy nanoparticles supported on CB with well-controlled particle size and alloy composition by the nanocapsule method (denoted as n-Pt_XCo/CB).[24−26] It was found in the temperature range from 30 to 70 °C that the value of apparent rate constant κ_{app} (per actual active surface area, a measure of j_S) for the ORR at X = 3 (d = 1.9 nm) was comparable to that for a $Pt_{68}Co_{32}$ thin film electrode, which was higher by a factor of 2.2 than that for a commercial standard Pt/CB (d = 2.6 nm, denoted as c-Pt/CB), corresponding to an increase in the MA

Received: October 5, 2012
Accepted: December 3, 2012
Published: December 12, 2012

by 3 times.[25] However, the κ_{app} values at both a bulk $Pt_{68}Co_{32}$ electrode and Pt_XCo/CB were found to decrease with increasing temperature above 70 °C and settled to nearly the same values as those for bulk Pt or c-Pt/CB.[19,25] It was concluded that the deactivation in the ORR could be ascribed with certainty to a dealloying of the nonprecious metal component (Co) in the hot acid solution, resulting in a thick Pt layer with bulk Pt-like properties. We consider that an essential point is the control of the formation of a stable, uniform, and thin Pt-skin layer, which can protect the underlying alloy from corrosion and maintain the modified electronic structure.

As an alternative way to further reduce the amount of Pt for the cathode catalyst, Adzic et al. have proposed Pt monolayer (Pt_{ML}) catalysts, which consist of a Pt_{ML} (equivalent to Pt-skin monolayer) deposited on core particles of Au, Pd, or Pd-alloys supported on CB.[27−30] In the preparation process, a monolayer of Cu (Cu_{ML}) was under-potentially deposited (UPD) on the core particles, followed by the galvanic displacement of the Cu_{ML} with a Pt_{ML}. These catalysts indeed exhibited high MA values for the ORR, e.g., about 3 to 5 times higher than that for c-Pt/CB. However, we must note two major drawbacks of these catalysts, i.e., an inherent dissolution of the Pd-core component, which decreases the durability, and the recent increase in the cost of Au (comparable to that of Pt). It is also difficult to cover the core-particles with the Pt_{ML} uniformly even by use of such a synthetic method.

The durability of all of these catalysts (Pt-alloys or Pt_{ML}-core) are, however, insufficient, because they have been supported on a CB such as Ketjenblack EC or Vulcan XC-72. It has been found that the c-Pt/CB cathode catalysts are severely degraded due to carbon corrosion at high potential, particularly during start−stop cycles or fuel starvation.[31−34] The corrosion of the carbon support leads to Pt catalyst particle sintering (agglomeration) and detachment from the surface,[35−41] as well as decreased integrity of the electronic conduction network in the catalyst layer, resulting in decreased ECA. Recently, we have succeeded in preparing monodisperse Pt nanoparticles supported on a graphitized carbon black (GCB), which exhibits higher resistance to carbon corrosion than a conventional CB, by the nanocapsule method (denoted as n-Pt/GCB).[42] We found that the n-Pt/GCB exhibited higher durability than those for c-Pt/CB and a commercial Pt/GCB (c-Pt/GCB), while maintaining a high MA, comparable to that for c-Pt/CB. Compared with the c-Pt/GCB, in which the Pt particles are segregated on the edges or grain boundaries of the GCB, n-Pt/GCB exhibited a remarkable advantage in mitigating both the GCB corrosion and the coarsening of the Pt. The most important factor leading to the high durability and high MA for the cathode catalysts was found to be the highly uniform distribution of monodisperse Pt nanoparticles over the whole surface of the GCB support, to which our nanocapsule method has contributed greatly.[43,44]

In the present research, we have developed a new catalyst with both high MA for the ORR (like n-Pt_XCo/CB) and high durability (like n-Pt/GCB). To protect the underlying Pt_XCo alloy from corrosion and maintain the modified electronic structure as stated above, we have deposited two monolayers of Pt-skin layer ($Pt_{2\ ML}$) on Pt_XCo core-particles (with uniform size and composition) and supported the $Pt_{2\ ML}$−Pt_XCo on GCB using a modified nanocapsule method. It was found that such a $Pt_{2\ ML}$-skin layer indeed contributed greatly to increasing both the MA and the durability of the new catalyst.

DESIGN OF STABILIZED Pt-SKIN LAYERS ON Pt−Co CORES HIGHLY DISPERSED ON GCB CATALYSTS

We have designed the stabilized Pt-skin layer/Pt−Co-core cathode catalyst in order to maintain both high MA and high durability, taking the stable structure of the catalyst particle, particle size, monodisperse state, and the GCB support material into account. First, we estimated the dependences of the MA on the size and composition of the catalyst particles. Assuming that the Pt−Co core particles have an ideal cuboctahedral shape and uniform alloy composition, we can calculate the number of atoms, N_{core}, contained in the core particle with the number of layers, L_{core}, from the following equation:[45,46]

$$N_{core} = \frac{10}{3}L_{core}^{\ 3} - 5L_{core}^{\ 2} + \frac{11}{3}L_{core} - 1 \quad (2)$$

As a measure of the particle size, we calculate d_{core} for a sphere having N_{core} atoms:

$$d_{core} = a_{PtCo}\left(\frac{3N_{core}}{2\pi}\right)^{1/3} \quad (3)$$

where a_{PtCo} is the lattice constant of the Pt−Co alloy.

Second, we considered the thickness of the stabilized Pt-skin layer prepared on the Pt−Co core particles. In order to reduce the total amount of Pt used and enhance the electronic modification effect by the underlying alloy, the Pt-skin layer should be prepared as thin as possible, i.e., a monolayer of Pt-skin (Pt_{ML}) is ideal. However, because the Pt_{ML} cannot completely cover the Pt−Co core, considering defect sites (steps, kinks, pits, or islands) on the top surface, the Pt_{ML}−Pt−Co is not so durable. Therefore, we have decided to prepare two monolayers of Pt-skin ($Pt_{2\ ML}$) on each core particle uniformly.

In our previous work,[25] it was found that Pt−Co alloy particles prepared by the nanocapsule method were in solid solution form, with a face-centered cubic (fcc) structure, but the change in the lattice constant of Pt−Co was smaller than that expected from Vegard's Law. This is because pure cobalt metal has a hexagonal closest packing (hcp) structure. The lattice constant of the $Pt_{50}Co_{50}$ alloy (50 atom % Co) was found to be smaller than that of pure Pt by only 3%. Here, we adopted $a_{PtCo} = a_{Pt}$ as the approximation that $Pt_{2\ ML}$ is formed epitaxially on the Pt−Co core, without any lattice mismatch. Then, we can calculate the total number of atoms, N_{total}, contained in the Pt−Co core covered with $Pt_{2\ ML}$ ($Pt_{2\ ML}$-Pt−Co) by substituting $L_{total} = L_{core} + 2$ into eq 2. The amount of Pt contained in the whole particle ($Pt_{2\ ML}$ + Pt in Pt−Co) can be thus calculated from eq 2. We also calculate the particle size of $Pt_{2\ ML}$−Pt−Co, d_{total}, for the sphere having N_{total} atoms similarly based on eq 3.

Next, we estimated the MA based on eq 1. Regarding the j_S for the $Pt_{2\ ML}$−Pt−Co, we have employed an enhancement factor compared with that of the c-Pt/CB (50 wt % Pt, d = 2.6 nm), $j_s/j_{s(Pt/CB)}$, ranging from 1.5 to 3.0 based on our results.[25] The value of ECA of the catalyst was calculated as the ideal specific surface area for spherical particles with size d_{total}. Figure 1 shows the enhancement factor of the mass activity compared with that of the c-Pt/CB, $MA_{Pt\text{-}PtCo}/MA_{Pt}$, as a function of d_{total} with the alloy core composition of Pt_XCo (X = 1 and 1/3). The values of $MA_{Pt\text{-}PtCo}/MA_{Pt}$, of course, increase with decreasing d_{total}. For example, at d_{total} = 2.5 nm, X = 1, and $j_s/j_{s(Pt/CB)}$ = 3.0, we can expect an MA of a factor of 3.6 higher than that for c-

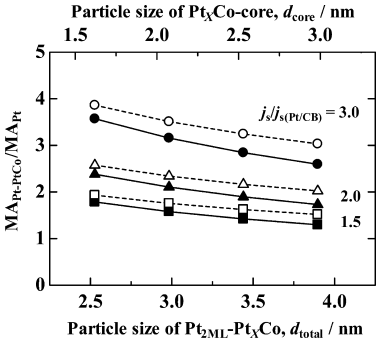

Figure 1. Enhancement factor of the mass activity compared with that for c-Pt/CB (50 wt % Pt, d = 2.6 nm), $MA_{Pt\text{-}PtCo}/MA_{Pt}$, as a function of d_{total} with the alloy core composition of Pt_XCo (X = 1, solid symbols; X = 1/3, open symbols). The enhancement factor compared with that for c-Pt/CB, $j_s/j_{s(Pt/CB)}$, was chosen as the parameter to be 1.5, 2.0, and 3.0. The particle diameter of Pt_XCo, d_{core}, ranging from 1.6 to 3.0 nm corresponds to the number of layers, L_{core}, from 4 to 7 (see eqs 2 and 3).

Pt/CB. A decrease in Pt content in the alloy-core from X = 1 to 1/3 could increase the value of $MA_{Pt\text{-}PtCo}/MA_{Pt}$ by a factor of ca. 1.2, but such a gain may be canceled by a decrease in the corrosion-resistance of the Co-rich alloy.[25] Therefore, we have first examined the use of PtCo (X = 1) particles as cores in the present research.

To increase the durability of the catalysts, the following factors should be taken into account. In addition to the use of the GCB support with higher resistance to carbon corrosion, the catalysts should be dispersed uniformly on the GCB support to reduce the corrosion current density (per area of GCB support covered with the catalysts).[42,44] Sufficient interparticle distance of the catalyst nanoparticles is effective in suppressing the coarsening by either sintering or so-called "electrochemical Ostwald ripening". It has also been reported that the monodisperse state of catalyst nanoparticles as in n-Pt/GCB[42,44] is effective in slowing down such degradation rates.[47−49]

EXPERIMENTAL SECTION

Preparation of Stabilized Pt-Skin Layers on PtCo-Core Nanoparticles. Scheme 1 illustrates a preparation protocol of a stable Pt-skin layer on PtCo alloy nanoparticles highly dispersed on graphitized carbon black (GCB) by a modified nanocapsule method, i.e., preparation of PtCo-core nanoparticles and formation of a stabilized Pt-skin layer on them, followed by supporting on GCB. First, the PtCo alloy nanoparticles were prepared by the nanocapsule method.[24,26] The chemical composition of the PtCo alloy and the particle size were controlled in the same manner as that described previously.[26] Platinum acetylacetonate, $Pt(acac)_2$, and cobalt acetylacetonate, $Co(acac)_3$, were dissolved in a mixed solvent of 1,2-hexadecanediol and diphenylether. The mixture was heated at 110 °C for 20 min in N_2 atmosphere with magnetic stirring, followed by the addition of a given amount of surfactant (oleic acid and oleylamine). The molar ratios of metal salts to surfactant (M/S) were adjusted to 0.1 and 0.5 in order to form PtCo particles with d_{core} of 2 and 3 nm, respectively.[26] The temperature was elevated to 220 °C and maintained constant for 30 min. Then, the reducing agent $LiBEt_3H$ was added dropwise into the mixture, followed by refluxing at 270 °C for 30 min. The suspension, consisting of PtCo alloy nanoparticles protected by organic surfactants, was cooled to room temperature.

In the second step, a stabilized Pt-skin layer was formed on the PtCo-core nanoparticles. A given amount of $Pt(acac)_2$, corresponding to $Pt_{2\ ML}$ on the PtCo-core, was enclosed by the surfactant (oleic acid and oleylamine) and mixed with the suspension of PtCo-core

Scheme 1. Illustration of the Preparation Protocol of the $Pt_{2\ ML}$−PtCo/GCB and PtCo/GCB Catalysts

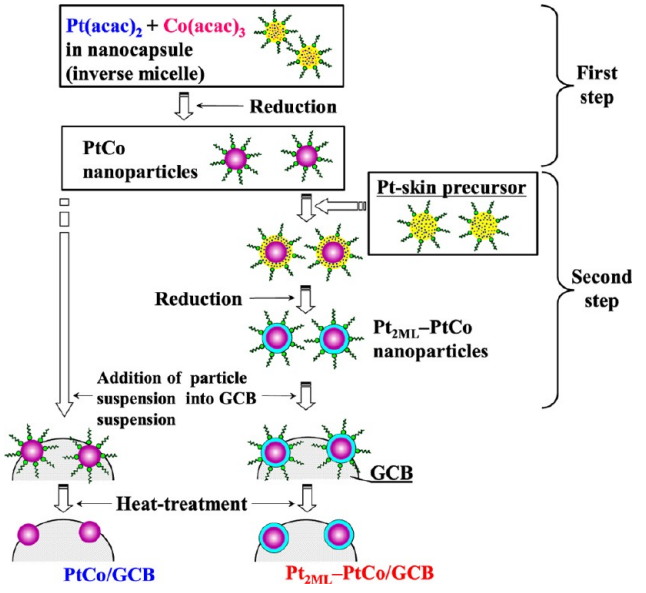

nanoparticles. After thorough magnetic stirring under N_2 atmosphere, $LiBEt_3H$ was added to form $Pt_{2\ ML}$ on the PtCo core, in a similar manner to that described above. In another flask, GCB powder (specific surface area = 150 $m^2\ g^{-1}$) was ultrasonically dispersed into diphenylether at ca. 30 °C. The mixture obtained above ($Pt_{2\ ML}$−PtCo nanoparticles protected by organic surfactants) was added dropwise into the GCB suspension, followed by elevating the temperature in a similar manner to that described previously.[26]

Finally, the mixture was cooled to room temperature and filtered. The powders were dried in vacuum and were heat-treated to remove the organic moieties completely.[26] For comparison purposes, PtCo/GCB (without stabilized $Pt_{2\ ML}$), n-Pt_3Co/GCB, and n-Pt/GCB catalysts were prepared by the conventional nanocapsule method.

Characterization and Electrochemical Measurement of the Catalysts. The $Pt_{2\ ML}$−PtCo/GCB and PtCo/GCB catalyst powders thus prepared were characterized by X-ray diffraction (XRD, Rigaku RINT2000) with Cu Kα radiation (50 kV, 300 mA) and spherical aberration (SA)-corrected scanning transmission electron microscope (STEM, Hitachi HD-2700, acceleration voltage = 200 and 80 kV) with an energy dispersive X-ray analyzer (EDX, Bruker Quantax). The minimum electron probe size for the observation was 0.2 nm. The loaded amounts of the metal catalysts on GCB support were quantified from the weight loss by combustion of the GCB at 600 °C in air.

Temperature dependences of the kinetically controlled ORR activities (j_k or MA_k) and H_2O_2 yield, $P(H_2O_2)$, on the $Pt_{2\ ML}$−PtCo/GCB catalysts were examined with use of the channel flow double electrode (CFDE) technique.[19,50,51] The CFDE cell includes a pair of planar electrodes: Au as the working electrode (flow direction length 1 mm × width 4 mm, geometric area 0.04 cm^2) and Pt as the collecting electrode in an electrolyte solution flow channel. From the hydrodynamic voltammograms under various laminar flow rates of the O_2-saturated 0.1 M $HClO_4$ electrolyte solution, we evaluated the j_k values at the working electrode, while the $P(H_2O_2)$ values were quantified at the collecting electrode, located downstream of the working electrode. In addition to the $Pt_{2\ ML}$−PtCo/GCB, n-Pt/GCB (47.9 wt %-Pt, d_{STEM} = 2.8 ± 0.4 nm) and n-Pt_3Co/GCB (45.6 wt %-metal, d_{STEM} = 3.2 ± 0.5 nm) catalysts, prepared by the nanocapsule method,[24,26] and c-Pt/CB (TEC10E50E, Tanaka Kikinzoku Kogyo, d = 2.6 nm) were employed for comparison purposes. The working electrode consisted of each catalyst uniformly dispersed on the Au substrate electrode at a constant loading of carbon support, 5.5 or 11.0 $\mu g\ cm^{-2}$, corresponding to one or two monolayers of catalyst supported on carbon, which enables an ideal, uniform flux of O_2 to be supplied to all of the catalyst agglomerates, with negligible

depletion.[51,52] Nafion film was coated on the catalyst layer with an average film thickness of 0.1 μm, which is thinner than the critical value reported for the ORR.[52] The Nafion-coated electrode was dried under nearly ethanol-saturated air at room temperature. Finally, the Nafion-coated electrode was heated at 130 °C for 30 min in air.

A Pt wire was used as the counter electrode. A reversible hydrogen electrode, which was maintained at the same temperature as that of the cell (t, °C) [denoted as RHE(t)], was used as the reference electrode. Hereinafter, all potentials will be referred to the RHE(t). Prior to the ORR measurements, Nafion-coated working electrodes were electrochemically stabilized by repetitive potential sweeping (typically 20 times) between 0.05 and 1.00 V in 0.1 M $HClO_4$ solution purged with N_2 gas. The purified electrolyte solution of 0.1 M $HClO_4$[53,54] was saturated with O_2 or N_2 gas by bubbling for at least 1 h prior to the electrochemical measurements. Hydrodynamic voltammograms at the working electrode under a flow of O_2-saturated 0.1 M $HClO_4$ solution (mean flow rate, 10−36 cm s^{-1}) were recorded by scanning its potential from 0.3 to 1.0 V at 0.5 mV s^{-1}. We have chosen the present experimental conditions carefully,[50−52] because it has been reported that the values of j_S or MA evaluated at 0.90 V on various catalysts at conventional scan rates of 5 to 20 mV s^{-1} for the positive-going scan decreased with decreasing scan rate.[55] By the use of the present slow scan rate (0.5 mV s^{-1}), together with the use of highly purified electrolyte solution, we confirmed that the current hysteresis of the positive-going and negative-going scans was negligibly small; i.e., we were able to observe the intrinsic activity of the catalyst examined under steady state condition.[50] To detect H_2O_2 emitted from the working electrode, the potential of the collecting electrode was set at 1.2 V. The collection efficiency (N) for the collecting electrode in the present CFDE was experimentally determined to be 0.28 ± 0.01.

RESULTS AND DISCUSSION

Characterization of $PtCo_{(2\ nm)}$/GCB and $Pt_{2\ ML}$−$PtCo_{(2\ nm)}$/GCB Catalysts. Figure 2 shows XRD patterns of the $PtCo_{(2\ nm)}$/GCB, $Pt_{2\ ML}$−$PtCo_{(2\ nm)}$/GCB, and n-Pt/GCB powders. XRD patterns of the $PtCo_{(3\ nm)}$/GCB and $Pt_{2\ ML}$−$PtCo_{(3\ nm)}$/GCB are also shown in Figure S1 of the Supporting Information. The broad peak at 2θ = ca. 25° for all samples was assigned to the (002) plane of GCB. The diffraction peaks of $PtCo_{(2\ nm)}$/GCB and $PtCo_{(3\ nm)}$/GCB identically shifted to higher angles than those of the fcc phase of pure Pt. No extra peaks assigned to Co or Co oxides nor those for the ordered alloys (PtCo or Pt_3Co) were identified. The average lattice constant of the PtCo catalyst calculated from (111), (200), (220), and (311) was 380 pm, which is smaller than that of pure Pt (392 pm) by ca. 3% and consistent with that of n-PtCo/CB.[25] Hence, the PtCo particles thus prepared are confirmed to be the solid solution with fcc structure. The diffraction peaks at the $Pt_{2\ ML}$−$PtCo_{(2\ nm)}$/GCB were located between those for the $PtCo_{(2\ nm)}$/GCB and pure Pt, and the shape of each peak was asymmetric. A similar XRD pattern was observed for $Pt_{2\ ML}$−$PtCo_{(3\ nm)}$/GCB. We will discuss the XRD patterns of the new catalysts later.

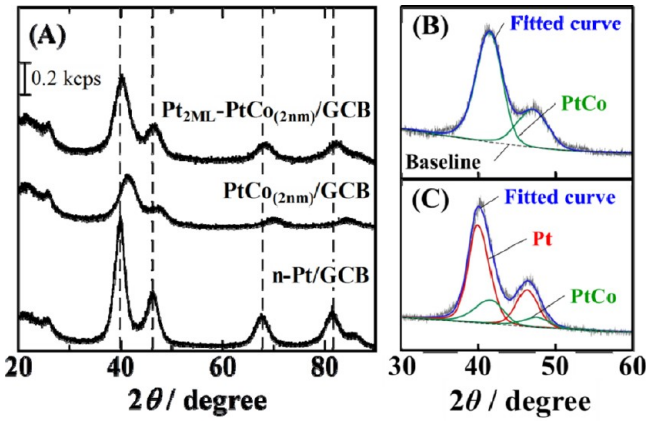

Figure 2. (A) X-ray diffraction patterns of $Pt_{2\ ML}$−$PtCo_{(2\ nm)}$/GCB and $PtCo_{(2\ nm)}$/GCB powders in comparison with n-Pt/GCB powder. Deconvolution of XRD peaks assigned to (111) and (200) (between 30 and 50°) of (B) $PtCo_{(2\ nm)}$/GCB and (C) $Pt_{2\ ML}$−$PtCo_{(2\ nm)}$/GCB. Curve-fitting in (C) was performed with both the full width at half-maximum (fwhm) and the peak position for PtCo fixed at the values obtained for (B) while allowing the fwhm for the Pt component (with identical peak position with that for n-Pt/GCB) and all peak heights to vary. Each fitting curve (blue) is the sum of the deconvoluted peaks.

Figure 3 shows STEM bright-field images of the $PtCo_{(2\ nm)}$/GCB and $Pt_{2\ ML}$−$PtCo_{(2\ nm)}$/GCB catalysts. High-angle annular dark-field (HAADF) images of the identical observation field are also shown in Figure S2 of the Supporting Information. The particle size distribution histograms among ca. 500 particles are also shown, based on the number of particles and the volume of particles in Figure 3B,E and C,F, respectively. Typical properties of these catalysts are summarized in Table 1. As reported previously, it is usually difficult to disperse Pt-based nanoparticles uniformly on GCB supports, which typically have smaller specific surface areas than those of the CBs; for example, many Pt particles were segregated on the edges or grain boundaries of the GCB support for a commercial c-Pt/GCB.[42−44] In contrast, similar to the case of n-Pt/GCB[42−44] or n-Pt_xCo/CB,[25,26] the nanocapsule method enables us to disperse the $PtCo_{(2\ nm)}$-core particles uniformly on the GCB support with a fairly narrow size distribution. The average particle size (d_{STEM} = 2.0 nm, based on the number of particles) was very close to that projected with a monodisperse state (very small standard deviation, σ_d = 0.2 nm). As shown in Figure S3 (Supporting Information), monodisperse $PtCo_{(3\ nm)}$-core particles were also prepared with d_{STEM} = 2.9 ± 0.2 nm on the GCB support. The composition of individual particles was analyzed by EDX for 20 particles randomly selected from each catalyst. The analyzed values of average composition of 46.5 atom %-Pt for $PtCo_{(2\ nm)}$ and 50.5 atom %-Pt for $PtCo_{(3\ nm)}$ were found to agree well with the starting atomic ratio of Pt−Co = 50:50 used for the preparation. The standard deviation in the composition among particles (σ_{comp}) was less than 3.3 atom % for both catalysts. Thus, monodisperse PtCo-core particles were successfully prepared with well-controlled average size (d_{STEM} = 2 and 3 nm) and alloy composition.

It was found in Figure 3E that the $Pt_{2\ ML}$−$PtCo_{(2\ nm)}$/GCB catalyst consisted of two kinds of particles with different d_{STEM} of ca. 3 nm (major peak) and 1.5 nm (minor peak). The former particles contained Pt and Co, whereas the latter were identified to be pure Pt (without Co) by EDX. The fraction of minor small Pt particles (d_{STEM} < 2 nm) was about 29% of the total number of particles. However, the volume fraction of such small Pt particles was only 4% of that for the whole set of particles (Figure 3F). A similar trend was seen for $Pt_{2\ ML}$−$PtCo_{(3\ nm)}$/GCB in Figure S3, Supporting Information. The value of d_{STEM} of the major large particles (more than 350 particles) was found to be 3.0 ± 0.4 nm, in good accord with that expected for the formation of the $Pt_{2\ ML}$ on the $PtCo_{(2\ nm)}$-core particles (see Figure 1). A similar increment in the d_{STEM} by 1 nm was seen for the preparation of the $Pt_{2\ ML}$ on the $PtCo_{(3\ nm)}$. It was also found for $Pt_{2\ ML}$−$PtCo_{(2\ nm)}$/GCB in Table 1 that the analyzed values of the loading level (44.4 wt

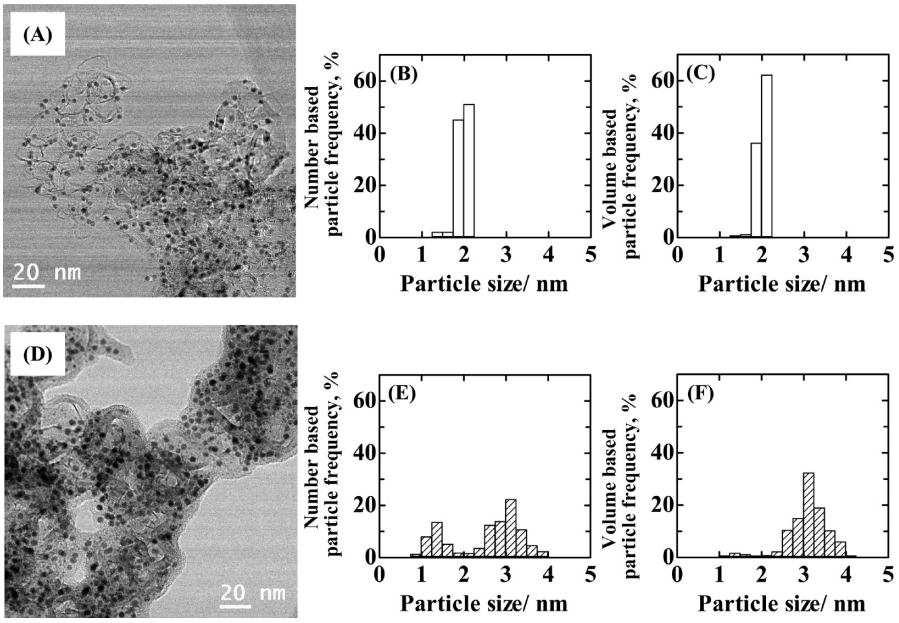

Figure 3. STEM bright-field images (acceleration voltage = 200 kV) of (A) $PtCo_{(2\ nm)}$/GCB and (D) $Pt_{2\ ML}$–$PtCo_{(2\ nm)}$/GCB. The particle size distribution histograms were obtained among ca. 500 particles in several images and are represented on the basis of the number of particles (B, E) and volume of particles (C, F); white bars, $PtCo_{(2\ nm)}$/GCB; hatched bars, $Pt_{2\ ML}$–$PtCo_{(2\ nm)}$/GCB.

Table 1. Typical Properties of Prepared $Pt_{2\ ML}$–$PtCo_{(2\ nm)}$/GCB Catalyst

composition of PtCo core particles[a]					composition of $Pt_{2\ ML}$–PtCo particles[a]	
Pt (atom %)	Co (atom %)	d_{STEM}[b] (nm)	layer number of Pt-skin	d_{STEM}[b] (nm)	Pt (atom %)	Co (atom %)
46.5 ± 3.2	53.5 ± 3.2	2.0 ± 0.2	2	3.0 ± 0.4	85.0 ± 2.8 (85.4)[c]	15.0 ± 2.8 (14.6)[c]

[a]Average composition and the standard deviations on the catalysts particles analyzed by spot-analysis with EDX at 20 particles randomly selected. [b]Average particle size and standard deviations, σ_d, based on the HAADF-STEM observation. [c]Projected compositions calculated assuming cuboctahedral shaped particles, eqs 2 and 3.

%) and the average composition (85.0 ± 2.8 atom %-Pt) for a 100 mg sample agreed well with the projected values, i.e., a metal loading level of 50 wt % and 85.4 atom %-Pt for the $Pt_{2\ ML}$–$PtCo_{(2\ nm)}$. A similar change in the composition was also observed for $Pt_{2\ ML}$–$PtCo_{(3\ nm)}$/GCB in Table S1, Supporting Information. These results strongly suggest that the Pt-skin precursor $Pt(acac)_2$ added in the second step in Scheme 1 was dominantly reduced on the top-surfaces of the PtCo-core particles to form $Pt_{2\ ML}$.

Figure 4 shows high resolution HAADF-STEM images of $PtCo_{(2\ nm)}$/GCB and $Pt_{2\ ML}$–$PtCo_{(2\ nm)}$/GCB. It was found for typical $PtCo_{(2\ nm)}$ particles (A1 and A2) that the intensity (brightness) was fairly uniform, suggesting a uniform elemental distribution of Pt and Co. Because HAADF-STEM images reflect the Z-contrast of materials, a pure Pt domain (such as $Pt_{2\ ML}$), if present, will have an intensity higher than that of the PtCo solid solution. For the particle B2 of $Pt_{2\ ML}$–$PtCo_{(2\ nm)}$, a relatively dark inner portion was found to be surrounded by a bright ring. A mosaic-like distribution of the intensity was observed for the particle B1.

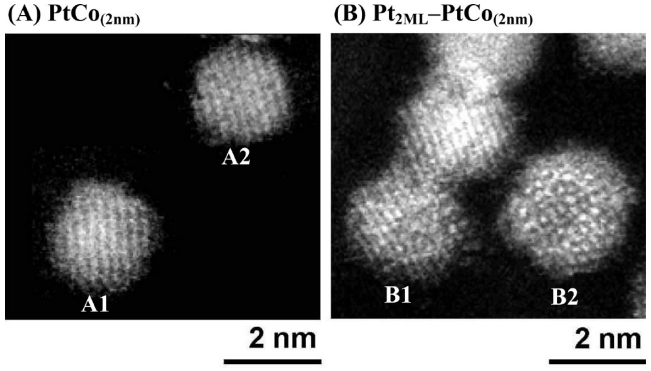

Figure 4. High resolution HAADF-STEM images of (A) $PtCo_{(2\ nm)}$ and (B) $Pt_{2\ ML}$–$PtCo_{(2\ nm)}$ particles.

Figure 5 shows HAADF-STEM images and the elemental distribution of Pt and Co obtained by EDX line scan analysis of the $PtCo_{(2\ nm)}$-core and $Pt_{2\ ML}$–$PtCo_{(2\ nm)}$ particles. The spot size of the electron beam was 0.3 nm. In order to mitigate the damage of the sample by the electron-beam as much as possible, the acceleration voltage and the emission current were set to 80 kV and 10 μA, respectively. It was found for several $PtCo_{(2\ nm)}$ particles that the distribution of Pt and Co was fairly uniform along with the analysis line for each particle. Both this result and the XRD pattern of $PtCo_{(2\ nm)}$/GCB in Figure 2 indicate that the pristine PtCo particles consisted of a uniform PtCo alloy solid solution without any Pt-skin layer, because the particles were not contacted with water or acid component.

In contrast, we have observed distinctly different elemental distributions of Pt and Co for $Pt_{2\ ML}$–$PtCo_{(2\ nm)}$. The signal intensity of Pt commenced to increase sharply from the edges of the particle, whereas the onset of Co signal intensity was just inside the particle, with a distance of 0.5 to 0.7 nm from the edge, corresponding to the thickness of the $Pt_{2\ ML}$. Similar

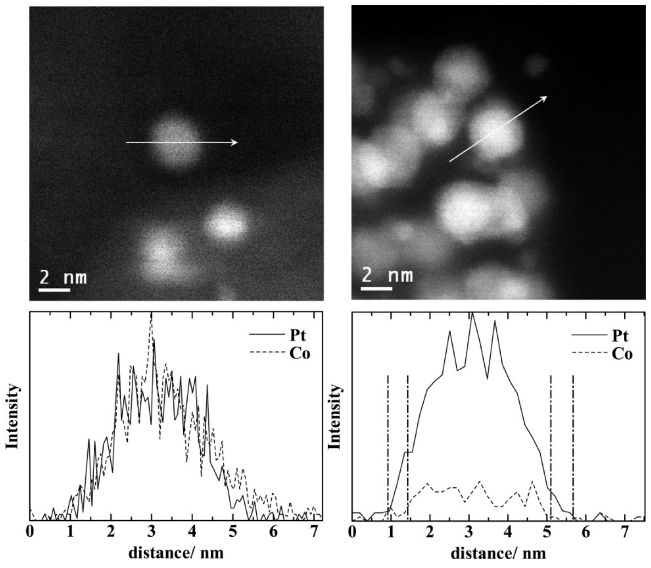

Figure 5. HAADF-STEM images and elemental distributions of Pt and Co obtained by EDX line scan analysis of $PtCo_{(2\ nm)}$-core (left) and $Pt_{2\ ML}$−$PtCo_{(2\ nm)}$ (right) particles.

trends for the distance between the onset positions of Pt and Co were observed for other $Pt_{2\ ML}$−$PtCo_{(2\ nm)}$ particles (see Figure S4, Supporting Information).

In addition to the characteristics of the $Pt_{2\ ML}$−PtCo particles stated above, we discuss the XRD patterns in Figure 2 and Figure S1 (Supporting Information) in detail. First, the diffraction peaks for both $PtCo_{(2\ nm)}$/GCB and $PtCo_{(3\ nm)}$/GCB were fitted well with a single component of the PtCo solid solution with fcc structure, as shown in Figure 2B and Figure S1B, Supporting Information. Second, as shown in Figure 2C, we have successfully deconvoluted the asymmetric diffraction peaks for $Pt_{2\ ML}$−$PtCo_{(2\ nm)}$/GCB into two components of pure Pt and PtCo with crystallite sizes of 2.8 nm (close to d_{STEM}) and 2.0 nm, respectively. Similar deconvolution results for $PtCo_{(3\ nm)}$/GCB are also shown in Figure S1C, Supporting Information. Thus, our characterization of $Pt_{2\ ML}$−PtCo/GCB indicates the formation of two monolayers of Pt-skin on the PtCo alloy solid solution.

ORR Activities and H_2O_2 Production Rate at Nafion-Coated $Pt_{2\ ML}$−PtCo/GCB Catalysts. Figure 6 shows the cyclic voltammograms (CVs) of the Nafion-coated $Pt_{2\ ML}$−$PtCo_{(2\ nm)}$/GCB, n-Pt_3Co/GCB (d_{STEM} = 3.2 nm), and n-Pt/GCB (d_{STEM} = 2.8 nm) electrodes in N_2-purged 0.1 M $HClO_4$ solution measured at 30 °C after the electrochemical

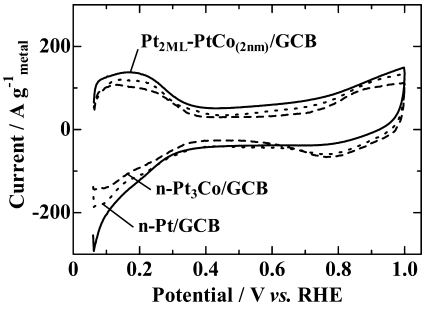

Figure 6. Cyclic voltammograms at Nafion-coated $Pt_{2\ ML}$−$PtCo_{(2\ nm)}$/GCB, n-Pt_3Co/GCB, and n-Pt/GCB electrodes in N_2-purged 0.1 M $HClO_4$ solution at 30 °C. The potential sweep rate was 0.1 V s^{-1}.

stabilization. The shape of the CV at the n-Pt_3Co/GCB electrode resembled that of n-Pt/GCB or polycrystalline Pt, indicating the spontaneous formation of a Pt-skin layer on the surface.[24,25] The shape of the CV at the $Pt_{2\ ML}$−$PtCo_{(2\ nm)}$/GCB electrode also resembled that of n-Pt/GCB, although the oxide formation/reduction peaks were somewhat smaller than those of n-Pt/GCB or n-Pt_3Co/GCB. The values of ECA were evaluated from the electric charge for the hydrogen adsorption wave Q_H in the CV, assuming Q_H° = 210 μC cm^{-2} for smooth polycrystalline Pt.[54,56] The values of ECA for the $Pt_{2\ ML}$−$PtCo_{(2\ nm)}$/GCB, n-Pt_3Co/GCB, and n-Pt/GCB electrodes were calculated to be 118, 89, and 80 m^2 g_{Pt}^{-1}, respectively. The values of the actual active surface area S on each electrode are also shown in the legend of Figure 7. The value of ECA for n-

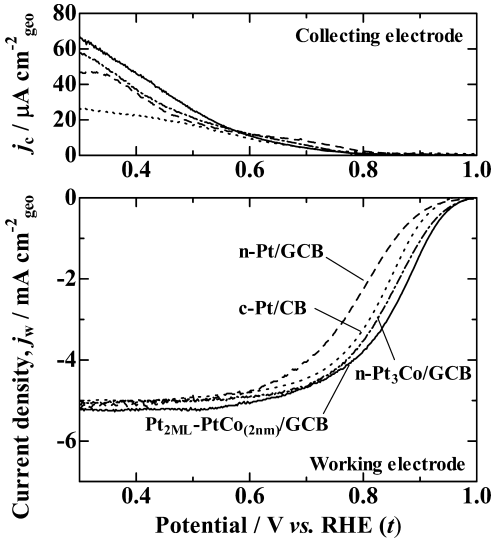

Figure 7. Hydrodynamic voltammograms for the ORR in O_2-saturated 0.1 M $HClO_4$ solution at Nafion-coated $Pt_{2\ ML}$−$PtCo_{(2\ nm)}$/GCB (S = 0.46 cm^2, 9.8 μg_{metal} cm^{-2}), n-Pt_3Co/GCB (S = 0.17 cm^2, 5.0 μg_{metal} cm^{-2}), n-Pt/GCB (S = 0.16 cm^2, 5.3 μg_{metal} cm^{-2}), and c-Pt/CB (S = 0.22 cm^2, 10.2 μg_{metal} cm^{-2}) electrodes at 30 °C, and simultaneously acquired current densities (j_c) on the Pt collecting electrode (at 1.2 V) for the oxidation of H_2O_2 (byproduct of the ORR at the working electrodes). The current densities j_w and j_c are normalized to the geometric area (0.04 cm^2). Potential scan rate = 0.5 mV s^{-1}. Mean flow rate of electrolyte U_m = 10 cm s^{-1}.

Pt_3Co/GCB is in accord with that calculated for spherical particles, and that of n-Pt/GCB is slightly smaller than the calculated value. In contrast, the ECA value of the $Pt_{2\ ML}$−$PtCo_{(2\ nm)}$/GCB electrode was larger by ca. 20% than that calculated for spherical particles of d_{total} = 3 nm (93 m^2 g_{Pt}^{-1}). This suggests that the Pt particles with d_{STEM} = 1.5 nm shown in Figure 3 (or Figure S2, Supporting Information) contributed to the ECA measured. We always checked the value of S after the hydrodynamic ORR measurement at a given temperature (30−100 °C).

Figure 7 shows hydrodynamic voltammograms for the ORR at these working electrodes in O_2-saturated 0.1 M $HClO_4$ solution at 30 °C at a mean solution flow rate U_m of 10 cm s^{-1} and simultaneously acquired currents at the Pt collecting electrode. The ORR currents at the $Pt_{2\ ML}$−$PtCo_{(2\ nm)}$/GCB and n-Pt_3Co/GCB catalysts commenced to increase at more positive potentials than that at n-Pt/GCB or c-Pt/CB by ca. 40 mV and reached diffusion limits at around 0.5 V. Small oxidation currents of H_2O_2 at the collecting electrodes were

dx.doi.org/10.1021/am302224n | ACS Appl. Mater. Interfaces 2012, 4, 6982−6991

observed for all catalysts at potentials less positive than ca. 0.9 V.

First, we discuss the H_2O_2 yield, $P(H_2O_2)$, defined as the percentage of H_2O_2 production rate to that of the overall ORR,

$$P(H_2O_2) = 2I_c/(N \times I_w + I_c) \times 100\% \quad (4)$$

where I_w and I_c are the currents at the working and collecting electrodes, respectively. As shown in Figure 8, the value of

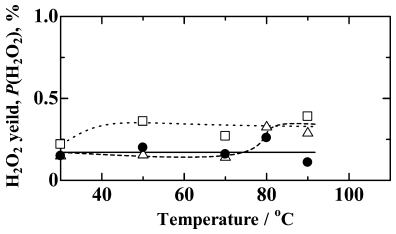

Figure 8. Temperature dependence of H_2O_2 yield at Nafion-coated $Pt_{2\ ML}$−$PtCo_{(2\ nm)}$/GCB (●), n-Pt_3Co/GCB (Δ), and n-Pt/GCB (□) electrodes at 0.80 V vs RHE(t). U_m = 36 cm s^{-1}.

$P(H_2O_2)$ from 30 to 70 °C at 0.80 V on both Nafion-coated n-Pt_3Co/GCB and $Pt_{2\ ML}$−$PtCo_{(2\ nm)}$/GCB was ca. 0.2%, which is smaller than that on n-Pt/GCB (ca. 0.4%). However, at temperatures higher than 80 °C, $P(H_2O_2)$ on n-Pt_3Co/GCB increased and reached the same value (ca. 0.4%) as that on n-Pt/GCB. In contrast, $P(H_2O_2)$ on $Pt_{2\ ML}$−$PtCo_{(2\ nm)}$/GCB maintained a very low level over the whole temperature range examined, which is favorable for mitigating the degradation of the polymer electrolyte membrane and gasket material. We will discuss the different temperature dependences of $P(H_2O_2)$ for $Pt_{2\ ML}$−$PtCo_{(2\ nm)}$/GCB and n-Pt_3Co/GCB in detail later.

The kinetically controlled current I_k at a given potential E was determined from the following equation:[57]

$$1/I = 1/I_k + 1/I_L = 1/I_k + 1/\{1.165 \times nF[O_2]w(U_m D^2 x_1^2/h)^{1/3}\} \quad (5)$$

where n, F, and $[O_2]$ are the number of electrons transferred, the Faraday constant, and the O_2 concentration in the bulk of the electrolyte solution, respectively; w, U_m, D, x_1, and h are the width of the working electrode, the mean flow rate of the electrolyte solution, the diffusion coefficient of O_2, the length of the working electrode in the electrolyte flow direction, and the half channel height, respectively. An example of I^{-1} vs $U_m^{-1/3}$ plots for the ORR on $Pt_{2\ ML}$−$PtCo_{(2\ nm)}$/GCB electrode is shown in Figure S5, Supporting Information. Linear relationships between I^{-1} and $U_m^{-1/3}$ were seen at all of the potentials examined, including 0.85, 0.80, 0.76, and 0.70 V at all of the electrodes. By extrapolating $U_m^{-1/3}$ to 0 (infinite flow rate), the value of I_k was calculated. Since the contribution of two-electron reduction to produce H_2O_2 to the overall ORR was very low (<0.4%) as stated above, we can also calculate an apparent rate constant κ_{app} at a constant overpotential η from the standard potential E° ($\eta = E - E^\circ$) over the whole operating temperature region from 30 to 90 °C, in the same manner as that described in our previous works,[25,51]

$$I_k/(4FS) = -\kappa_{app}[H^+][O_2] \quad (6)$$

where $[H^+]$ is the bulk concentration of H^+ (0.1 M) and S is the actual active surface area of the catalyst.

Figure 9 shows Arrhenius plots for the κ_{app} per real surface area at 0.85 V at various Nafion-coated electrodes. For n-Pt/

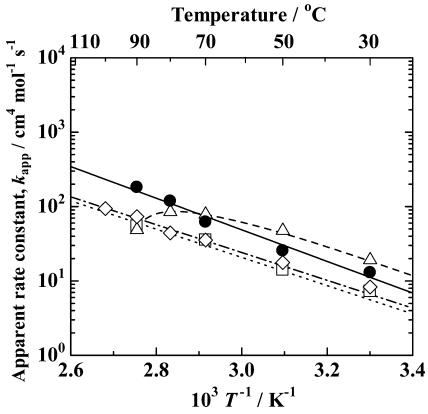

Figure 9. Arrhenius plots of apparent rate constant κ_{app} for the ORR at Nafion-coated $Pt_{2\ ML}$−$PtCo_{(2\ nm)}$/GCB (●), n-Pt_3Co/GCB (Δ), n-Pt/GCB (□), and c-Pt/CB (◊) electrodes. The overpotential of −0.435 V vs E° corresponds to 0.85 V vs RHE at 30 °C. Because the E° and E[RHE(t)] shift to less positive values in a different manner, the corrected potential E was applied so as to maintain a constant overpotential. The values of κ_{app} for the n-Pt/GCB and c-Pt/CB are cited from our previous work.[43,51]

GCB and c-Pt/CB, linear relationships between log κ_{app} and $1/T$, corresponding to the Arrhenius equation, $\kappa_{app} = Z \exp(-\varepsilon_a/RT)$ with an activation energy of ca. 40 kJ mol^{-1},[43,46,51] were observed. The values of κ_{app} at the Nafion-coated n-Pt/GCB electrode agreed beautifully with those of c-Pt/CB.[43] The temperature-dependence of κ_{app} on n-Pt_3Co/GCB was very similar to that of n-Pt_3Co/CB reported previously.[25] In the low temperature region between 30 and 50 °C, the value of κ_{app} on n-Pt_3Co/GCB was larger than that on c-Pt/CB by a factor of 2, but κ_{app} rather decreased with increasing temperature above 80 °C, settling at a value nearly identical with that for c-Pt/CB at 90 °C. The change in $P(H_2O_2)$ on n-Pt_3Co/GCB with temperature in Figure 8 also suggests that the surface of the n-Pt_3Co particles became more "Pt-like". Therefore, a severe dealloying of the Co component in the hot acid solution (>70 °C) could result in the formation of a thicker Pt layer, the electronic state of which is no longer affected by the underlying alloy.[19,25]

In contrast, for $Pt_{2\ ML}$−$PtCo_{(2\ nm)}$/GCB, a good linear relationship between log κ_{app} and $1/T$ was observed between 30 and 90 °C, without any deactivation effect observed at n-Pt_3Co/GCB. Thus, the value of κ_{app} on $Pt_{2\ ML}$−$PtCo_{(2\ nm)}$/GCB was 1.8 times larger than that on c-Pt/CB over the whole temperature range examined. Such a distinct enhancement in the κ_{app} for the ORR up to high temperature is what we expected for the $Pt_{2\ ML}$−$PtCo_{(2\ nm)}$/GCB.

Furthermore, we evaluated the values of kinetically controlled mass activity MA_k (I_k divided by the mass of Pt, m_{Pt}) on these catalysts in O_2-saturated 0.1 M $HClO_4$. The value of MA_k is regarded as the maximum MA for a particular catalyst with maximal electrolyte wetting, at a sufficiently high potential (0.85−0.90 V) to avoid mass transport limitations. We have proposed the effectiveness of Pt (Ef_{Pt}), which is defined as the ratio of MA in the membrane-electrode-assembly (MEA) to the MA_k based on the CFDE measurements [Ef_{Pt} (%) = (MA/MA_k) × 100].[58,59] Up to now, it has been common to evaluate the MA at 0.90 V for conventional MEAs, e.g., with 0.40 mg_{Pt}

cm^{-2} loading operated with fully humidified (100% RH) air and 150 $kPa_{absolute}$.[55] However, for MEAs with a reduced Pt loading of 0.04 mg_{Pt} cm^{-2} operated under low humidity (30%RH) and ambient pressure,[59] the current observed at 0.90 V has not always been completely kinetically controlled due to an increased contribution of oxidation current for H_2 diffusing through the membrane from the anode to the cathode. Since the currents at 0.85 V for such MEAs are so sufficiently low that there is little mass transport limitation, we have judged that the MA measured at 0.85 V is more appropriate, considering the actual stringent operating conditions for PEFCs.

Figure 10 shows the MA_k values at 0.85 V on various catalysts in O_2-saturated 0.1 M $HClO_4$ as a function of

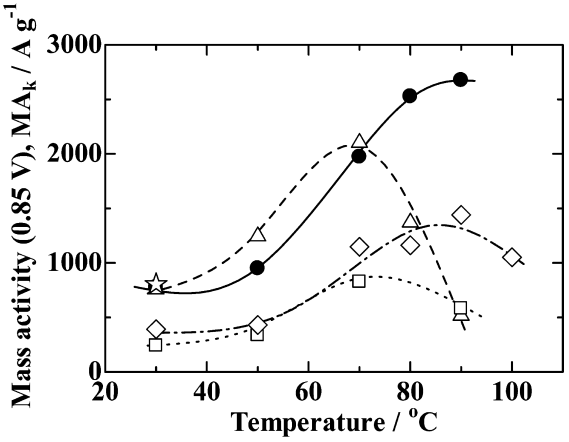

Figure 10. Temperature dependence of the kinetically controlled mass activities MA_k at 0.85 V vs RHE for the ORR at Nafion-coated $Pt_{2\ ML}$–$PtCo_{(2\ nm)}$/GCB (●), $Pt_{2\ ML}$–$PtCo_{(3\ nm)}$/GCB (star),n-Pt_3Co/GCB (Δ), n-Pt/GCB (□), and c-Pt/CB (◊) electrodes in O_2-saturated 0.1 M $HClO_4$ solution. $MA_k = I_k/m_{Pt} = -4F\kappa_{app}[H^+][O_2] \times ECA$.

temperature. Except for the case of n-Pt_3Co/GCB, the MA_k values increased with temperature and leveled off or decreased slightly at high temperatures >90 °C. This is mainly because the increase in the κ_{app} with temperature was canceled by the decrease in the concentration of O_2, $[O_2]$, dissolved in the electrolyte solution (see eq 6). Although the n-Pt_3Co/GCB exhibited the highest MA_k up to 70 °C, its durability was insufficient, because the nonuniform Pt-skin layer cannot suppress the dissolution of the underlying alloy at high temperatures. In contrast, the newly developed $Pt_{2\ ML}$–$PtCo_{(2\ nm)}$/GCB exhibited a MA_k value larger than that for the c-Pt/CB catalyst over whole temperature range. The MA_k value for $Pt_{2\ ML}$–$PtCo_{(2\ nm)}$/GCB at 80 and 90 °C was about two times larger than that for c-Pt/CB. The MA_k value for $Pt_{2\ ML}$–$PtCo_{(3\ nm)}$/GCB at 30 °C was also two times larger than that for c-Pt/CB, but we did not carry out the test at higher temperature in the present work. These enhancement factors of MA_k were comparable to the expected value of $MA_{Pt\text{-}PtCo}/MA_{Pt}$ calculated by the cuboctahedral model shown in Figure 1 with the experimental values of $j_s/j_{s(Pt/CB)} = 1.8$ (see Figure 9) and $d_{total} = 3$ nm.

It should be noted that the MA_k on n-Pt/GCB at 90 °C became lower than that on c-Pt/CB, even though the κ_{app} in Figure 9 was identical with that of c-Pt/CB. We indeed observed a decrease in the ECA in the CV for n-Pt/GCB after the ORR measurement at 90 °C, probably due to the Pt coarsening. Figure 11 shows HAADF-STEM images and particle size distribution histograms based on the number of

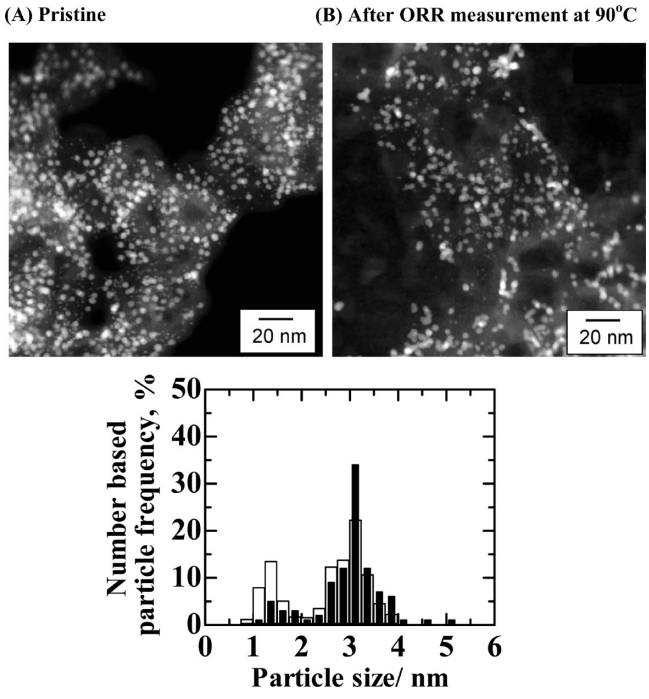

Figure 11. HAADF-STEM images of the $Pt_{2\ ML}$–$PtCo_{(2\ nm)}$/GCB: (A) pristine and (B) after ORR measurement at 90 °C. The particle size distribution histograms were obtained among ca. 500 particles in several images and are represented on the basis of the number of particles; white bars, pristine; black bars, after the ORR measurement at 90 °C.

particles of the $Pt_{2\ ML}$–$PtCo_{(2\ nm)}$/GCB catalysts after the ORR measurements at 90 °C. The average size (d_{STEM} = ca. 3 nm) and size distribution of the major particles were almost unchanged, whereas the fraction of small pure Pt particles decreased from 29 to 13% (4 to 2 vol %), probably due to a dissolution of such Pt particles in the electrolyte solution at high temperature. However, the amount of Pt dissolved was very small compared to the whole mass of particles. Even if such a small amount (2 vol %) of Pt ions were to redeposit on the $Pt_{2\ ML}$–$PtCo_{(2\ nm)}$ particles by so-called "Ostwald ripening", the increase in the Pt layer thickness was estimated to be only 0.05 monolayer. Hence, it is clearly shown that the enhancement in the MA_k for the ORR of the $Pt_{2\ ML}$–$PtCo_{(2\ nm)}$/GCB up to high temperature can be confidently ascribed to the intentionally formed $Pt_{2\ ML}$ on PtCo alloy nanoparticles. Furthermore, we have found a superior durability of $Pt_{2\ ML}$–$PtCo_{(2\ nm)}$/GCB in a preliminary durability test by potential-step cycle between 0.9 and 1.3 V (holding 30 s at each E, 1 min for one cycle, simulating the start–stop cycles in FCEVs) in N_2-purged 0.1 M $HClO_4$ solution at 25 °C;[60] i.e., the number of potential step cycles, at which the slowly decreasing ECA for the $Pt_{2\ ML}$–$PtCo_{(2\ nm)}$/GCB reached one-half of the initial level, was ca. 100 times larger than that for n-Pt/GCB. This suggests that the $Pt_{2\ ML}$–$PtCo_{(2\ nm)}$ nanoparticles exhibited higher durability than pure Pt in spite of the use of the identical GCB support. Durability tests (changes in ECA and ORR activity for start–stop cycles and load-change cycles) of these catalysts in a practical temperature range for PEFCs (30–100 °C) are in progress in our laboratory.

dx.doi.org/10.1021/am302224n | ACS Appl. Mater. Interfaces 2012, 4, 6982–6991

CONCLUSIONS

We have succeeded in preparing new cathode catalysts, which consist of two monolayers of Pt deposited on PtCo-alloy particles of fcc solid solution (with uniform size and composition) supported on GCB by a modified nanocapsule method. The value of H_2O_2 yield on $Pt_{2\ ML}$−$PtCo_{(2\ nm)}$/GCB in the ORR was very small (0.2%), which was about one-half that on c-Pt/CB; this is favorable for mitigating the degradation of the polymer electrolyte membrane and gasket material. The values of κ_{app} on the Nafion-coated $Pt_{2\ ML}$−$PtCo_{(2\ nm)}$/GCB were found to be 1.8 times larger than that on the standard commercial c-Pt/CB and increased with temperature in the Arrhenius-type relation between 30 and 90 °C, without any deactivation effect, unlike n-Pt_3Co/GCB. We also found that MA_k for the ORR on the $Pt_{2\ ML}$−$PtCo_{(2\ nm)}$/GCB catalyst exhibited a ca. two times larger value than that on the c-Pt/CB catalyst over the whole temperature range. Such an enhanced ORR activity of the $Pt_{2\ ML}$−$PtCo_{(2\ nm)}$/GCB catalyst was due to the modified electronic state at the $Pt_{2\ ML}$ by the underlying PtCo alloy. The high durability of this catalyst was also suggested by a preliminary test. The MA for the ORR, as well as the durability, can be increased further by controlling the composition of the Pt−Co alloy and/or reaction conditions.

ASSOCIATED CONTENT

Supporting Information

X-ray diffraction patterns of $Pt_{2\ ML}$−$PtCo_{(3\ nm)}$/GCB, HAADF-STEM images of $PtCo_{(2\ nm)}$/GCB and $Pt_{2\ ML}$−$PtCo_{(2\ nm)}$/GCB, TEM images and particle size distribution histograms of $Pt_{2\ ML}$−$PtCo_{(3\ nm)}$/GCB, typical properties of $Pt_{2\ ML}$−$PtCo_{(3\ nm)}$/GCB, elemental distribution of Pt and Co for some particles of $Pt_{2\ ML}$−$PtCo_{(2\ nm)}$/GCB, and I^{-1} vs $U_m^{-1/3}$ plots obtained from hydrodynamic voltammograms for the ORR. This material is available free of charge via the Internet at http://pubs.acs.org.

AUTHOR INFORMATION

Corresponding Author

*Phone: +81-55-220-8619. Fax: +81-55-220-8618. E-mail: h-uchida@yamanashi.ac.jp.

Notes

The authors declare no competing financial interest.

ACKNOWLEDGMENTS

This work was supported by the funds for the "Research on Nanotechnology for High Performance Fuel Cells" (HiPer-FC) project from the New Energy and Industrial Technology Development Organization (NEDO) of Japan.

REFERENCES

(1) Mukerjee, S.; Srinivasan, S.; Soriaga, M. P.; McBreen, J. *J. Electrochem. Soc.* **1995**, *142*, 1409−1422.
(2) Toda, T.; Igarashi, H.; Watanabe, M. *J. Electroanal. Chem.* **1999**, *460*, 258−262.
(3) Toda, T.; Igarashi, H.; Uchida, H.; Watanabe, M. *J. Electrochem. Soc.* **1999**, *146*, 3750−3756.
(4) Toda, T.; Honma, I. *Trans. Mater. Res. Soc. Jpn.* **2003**, *28*, 215−220.
(5) Xiong, L.; Manthiram, A. *Electrochim. Acta* **2005**, *50*, 2323−2329.
(6) Mukerjee, S.; Srinivasan, S. *J. Electroanal. Chem.* **1993**, *357*, 201−224.
(7) Min, M. K.; Cho, J.; Cho, K.; Kim, H. *Electrochim. Acta* **2000**, *45*, 421−4217.
(8) Neergat, M.; Shukla, A. K.; Gandhi, K. S. *J. Appl. Electrochem.* **2001**, *31*, 373−378.
(9) Stamenković, V.; Schmidt, T. J.; Ross, P. N.; Marković, N. M. *J. Phys. Chem. B* **2002**, *106*, 11970−11979.
(10) Rao, C. V.; Reddy, A. L. M.; Ishikawa, Y.; Ajayan, P. M. *Carbon* **2011**, *49*, 931−936.
(11) Drillet, J. F.; Ee, A.; Friedemann, J.; Kötz, R.; Schnyder, B.; Schmidt, V. M. *Electrochim. Acta* **2002**, *47*, 1983−1988.
(12) Stamenković, V.; Schmidt, T. J.; Ross, P. N.; Marković, N. M. *J. Electroanal. Chem.* **2003**, *554*−*555*, 191−199.
(13) Yang, H.; Vogel, W.; Lamy, C.; Alonso-Vante, N. *J. Phys. Chem. B* **2004**, *108*, 11024−11034.
(14) Tamizhmani, G.; Capuano, G. A. *J. Electrochem. Soc.* **1994**, *141*, 968−975.
(15) Paffett, M. T.; Beery, J. G.; Gottesfeld, S. *J. Electrochem. Soc.* **1988**, *135*, 1431−1436.
(16) Antolini, E.; Passos, R. R.; Ticianelli, E. A. *Electrochim. Acta* **2002**, *48*, 263−270.
(17) Wan, L.-J.; Moriyama, T.; Ito, M.; Uchida, H.; Watanabe, M. *Chem. Commun.* **2002**, 58−59.
(18) Uchida, H.; Ozuka, H.; Watanabe, M. *Electrochim. Acta* **2002**, *47*, 3629−3636.
(19) Wakabayashi, N.; Takeichi, M.; Uchida, H.; Watanabe, M. *J. Phys. Chem. B* **2005**, *109*, 5836−5841.
(20) Wakisaka, M.; Mitsui, S.; Hirose, Y.; Kawashima, K.; Uchida, H.; Watanabe, M. *J. Phys. Chem. B* **2006**, *110*, 23489−23496.
(21) Stamenkovic, V. R.; Mun, B. S.; Mayrhofer, K. J. J.; Ross, P. N.; Markovic, N. M. *J. Am. Chem. Soc.* **2006**, *128*, 8813−8819.
(22) Watanabe, M.; Uchida, H. *Fuel Cell Catalysis: A Surface Science Approach*; Koper, M. T. M., Ed.; Wiley: Hoboken, NJ, 2009, p 317−341.
(23) Wakisaka, M.; Uchida, H.; Watanabe, M. *Fuel Cell Science: Theory, Fundamentala, and Biocatalysis*; Wieckowski, A., Norskov, J., Eds.; Wiley: Hoboken, NJ, 2010, p 147−168.
(24) Yano, H.; Kataoka, M.; Yamashita, H.; Uchida, H.; Watanabe, M. *Langmuir* **2007**, *23*, 6438−6445.
(25) Yano, H.; Song, J. M.; Uchida, H.; Watanabe, M. *J. Phys. Chem. C* **2008**, *112*, 8372−8380.
(26) Okaya, K.; Yano, H.; Uchida, H.; Watanabe, M. *ACS Appl. Mater. Interfaces* **2010**, *2*, 888−895.
(27) Zhang, J.; Lima, F. H. B.; Shao, M. H.; Sasaki, K.; Wang, J. X.; Hanson, J.; Adzic, R. R. *J. Phys. Chem. B* **2005**, *109*, 22701−22704.
(28) Shao, M. H.; Huang, T.; Liu, P.; Zhang, J.; Sasaki, K.; Vukmirovic, M. B.; Adzic, R. R. *Langmuir* **2006**, *22*, 10409−10415.
(29) Shao, M. H.; Sasaki, K.; Marinkovic, N. S.; Zhang, L.; Adzic, R. R. *Electrochem. Commun.* **2007**, *9*, 2848−2853.
(30) Wang, J. X.; Inada, H.; Wu, L.; Zhu, Y.; Choi, Y.; Liu, P.; Zhou, W.-P.; Adzic, R. R. *J. Am. Chem. Soc.* **2009**, *131*, 17298−17302.
(31) Reiser, C. A.; Bregoli, L.; Patterson, T. W.; Yi, J. S.; Yang, J. D.; Perry, M. L.; Jarvi, T. D. *Electrochem. Solid-State Lett.* **2005**, *8*, A273−A276.
(32) Tang, H.; Qi, Z.; Ramani, M.; Elter, J. F. *J. Power Sources* **2006**, *158*, 1306−1312.
(33) Meyers, J. P.; Darling, R. M. *J. Electrochem. Soc.* **2006**, *153*, A1432−A1442.
(34) Yu, X.; Ye, S. *J. Power Sources* **2007**, *172*, 145−154.
(35) Wilson, M. S.; Garzon, F. H.; Sickafus, K. E.; Gottesfeld, S. *J. Electrochem. Soc.* **1993**, *140*, 2872−2877.
(36) Darling, R. M.; Meyers, J. P. *J. Electrochem. Soc.* **2003**, *150*, A1523−A1527.
(37) Ferreira, P. J.; la O, G. J.; Shao-Horn, Y.; Morgan, D.; Makharia, R.; Kocha, S.; Gasteiger, H. A. *J. Electrochem. Soc.* **2005**, *152*, A2256−A2271.
(38) Xie, J.; Wood, D. L.; Wayne, D. M.; Zawodzinski, T. A.; Atanassov, P.; Borup, R. L. *J. Electrochem. Soc.* **2005**, *152*, A104−A113.
(39) Stevens, D. A.; Hicks, M. T.; Haugen, G. M.; Dahn, J. R. *J. Electrochem. Soc.* **2005**, *152*, A2309−A2315.
(40) Patterson, T. W.; Darling, R. M. *Electrochem. Solid-State Lett.* **2006**, *9*, A183−A185.

(41) Yoda, T.; Uchida, H.; Watanabe, M. *Electrochim. Acta* **2007**, *52*, 5997−6005.
(42) Yano, H.; Akiyama, T.; Bele, P.; Uchida, H.; Watanabe, M. *Phys. Chem. Chem. Phys.* **2010**, *12*, 3806−3014.
(43) Yano, H.; Akiyama, T.; Uchida, H.; Watanabe, M. *Energy Environ. Sci.* **2010**, *3*, 1511−1514.
(44) Yano, H.; Akiyama, T.; Uchida, H.; Watanabe, M. *J. Electroanal. Chem.*, in press, DOI: 10.1016/j.jelechem.2012.09.028.
(45) Van der Klink, J. J.; Brom, H. B. *Prog. Nucl. Magn. Reson. Spectrosc.* **2000**, *36*, 89−201.
(46) Yano, H.; Inukai, J.; Uchida, H.; Watanabe, M.; Babu, P. K.; Kobayashi, T.; Chung, J. H.; Oldfield, E.; Wieckowski, A. *Phys. Chem. Chem. Phys.* **2006**, *8*, 4932−4939.
(47) Takeshita, T.; Murata, H.; Hatanaka, T.; Morimoto, Y. *ECS Trans.* **2008**, *16*, 367−373.
(48) Hatanaka, T.; Takeshita, T.; Murata, H.; Hasegawa, N.; Asano, T.; Kawasumi, M.; Morimoto, Y. *ECS Trans.* **2008**, *16*, 1961−1965.
(49) Trogadas, P.; Fuller, T. F. *ECS Trans.* **2011**, *41*, 761−773.
(50) Wakabayashi, N.; Takeichi, M.; Itagaki, M.; Uchida, H.; Watanabe, M. *J. Electroanal. Chem.* **2005**, *574*, 339−346.
(51) Yano, H.; Higuchi, E.; Uchida, H.; Watanabe, M. *J. Phys. Chem. B* **2006**, *110*, 16544−16549.
(52) Higuchi, E.; Uchida, H.; Watanabe, M. *J. Electroanal. Chem.* **2005**, *583*, 69−76.
(53) Watanabe, M.; Motoo, S. *J. Electroanal. Chem. Interfacial Electrochem.* **1975**, *60*, 259−266.
(54) Uchida, H.; Ikeda, N.; Watanabe, M. *J. Electroanal. Chem.* **1997**, *424*, 5−12.
(55) Gasteiger, H. A.; Kocha, S. S.; Sompalli, B.; Wagner, F. T. *Appl. Catal., B: Environ.* **2005**, *56*, 9−35.
(56) Watanabe, M.; Motoo, S. *J. Electroanal. Chem. Interfacial Electrochem.* **1975**, *60*, 275−283.
(57) Uchida, H.; Izumi, K.; Aoki, K.; Watanabe, M. *Phys. Chem. Chem. Phys.* **2009**, *11*, 1771−1779.
(58) Lee, M.; Uchida, M.; Yano, H.; Tryk, D. A.; Uchida, H.; Watanabe, M. *Electrochim. Acta* **2010**, *55*, 8504−8512.
(59) Lee, M.; Uchida, M.; Tryk, D. A.; Uchida, H.; Watanabe, M. *Electrochim. Acta* **2011**, *56*, 4783−4790.
(60) http://fccj.jp/pdf/19_01_kt.pdf.